Fuller, J. D., Jalalvand, M., & Wisnom, M. R. (2016). Combining fibre rotation and fragmentation to achieve pseudo-ductile CFRP laminates. *Composite Structures*, *142*, 155-166. https://doi.org/10.1016/j.compstruct.2016.01.073

Combining fibre rotation and fragmentation to achieve pseudo-ductile CFRP laminates

J.D. Fuller, M. Jalalvand, M.R. Wisnom

Advanced Composites Centre for Innovation and Science, University of Bristol, Queen's Building, Bristol, BS8 1TR

Abstract

The pseudo-ductility shown by thin ply angle-ply laminates has been coupled with the gradual fragmentation of unidirectional (0°) plies to yield a metal-like stress-strain curve for a $[\pm\theta_{\mathrm{m}}/0_{\mathrm{n}}]_{\mathrm{s}}$ laminate. This has led to a significant increase in pseudo-ductility than either angle-ply fibre rotation or 0° fragmentation have shown previously. Analytical modelling has been developed that accounts for the damage processes that contribute to the gradual failure of the 0° plies and predictions have been made taking into account the fragmentation, delamination and eventual failure of the laminate. Experimental results are shown to correlate well with the modelling, despite some variability in the responses. Analysis via X-ray computed tomography of tested specimens shows the progression of the fragmentation and delamination damage modes prior to laminate failure and provides an in-depth understanding of the process that leads to the demonstrated pseudo-ductile strains.

Keywords: Thin ply, Gradual failure, Delamination, Analytical modelling

1. Introduction

Carbon fibre reinforced polymer (CFRP) composites have excellent specific strength and stiffness properties, but tend to be limited by their linear-elastic stress-strain response and sudden, catastrophic failure. This lack of ductility greatly limits the structural efficiency of a CFRP design. Recently, interest in improving the ductility of high performance composites has increased.

Studies have covered a variety of approaches, including metal-reinforced, metal hybrid and self-reinforced composites [**?** **?** **?** **?** **?** **?**] and braided laminates [**?** **?**] to achieve ductility or pseudo-ductility. The approaches that incorporate steel fibres [**?** **?**] and thin steel layers [**?**] in a metal-hybrid polymer composite, take advantage of the inherent ductility of the metal to provide the non-linearity. In particular, the work by Masania et al. [**?**] involved improving the stress redistribution at holes and bolted joints in composite parts. Steel foil replaced the outer 90° plies in a $[90/45/0/-45]_{\mathrm{s}}$ CFRP laminate. After open hole tension and double-lap shear tests, the inclusion of the steel foil led to increased non-linearity and an improvement in both open-hole and bearing strength when compared to the baseline CFRP laminate. The improvements in ductility via use of steel foil or fibres are offset by the relatively low yield and failure stresses demonstrated, which is seen also in

*Corresponding author

self-reinforced composites that use polypropylene or polyethylene terephthalate fibres [**?** **?**]. Braided composites present another opportunity to develop ductile composites. Work by Gautam et al. [**?**] has shown that a tubular braided CFRP composite can exhibit considerable non-linearity, even when flattened. Biaxial specimens of $\pm 35°$, $\pm 45°$ and $\pm 55°$ were tested under a uniaxial tensile load, showing increasing pseudo-ductility with fibre angle. It was also found, however, that initial modulus and 'yield' strength decreased sharply with increased fibre angle. The specimens demonstrated a large amount of necking prior to failure, suggesting significant geometrical rearrangement.

Work conducted as part of the High Performance Ductile Composite Technologies (HiPerDuCT) programme grant, has shown that it is possible to produce highly non-linear stress-strain responses with spread-tow thin ply laminates [**?** **?** **?** **?** **?** **?** **?**]. Studies conducted by Fuller and Wisnom [**?** **?**] on thin ply angle-ply laminates have shown high pseudo-ductile strains and strengths, through fibre rotation and matrix plasticity. For example, $[\pm 25_5]_\mathrm{s}$ laminates (ply thickness, $t_\mathrm{p} = 0.03\,mm$) have shown experimental strength, σ_x^*, of 950 MPa, laminate failure strain, ϵ_x^*, of 3.60% and a pseudo-ductile strain, ϵ_d, of 1.22%. Pseudo-ductility in this case is defined as the laminate failure strain minus the strain at the same stress level on a straight line of the initial modulus. These mechanisms are effectively allowed to occur due to the suppression of matrix cracking and free-edge delaminations — the damage mechanisms that normally cause premature failure in angle-ply laminates. The stress at which these damage mechanisms initiate and propagate has been previously shown to be inversely proportional to ply thickness [**?** **?** **?** **?** **?** **?** **?**]. In particular, Wang et al. [**?**], Leguillon et al. [**?**] and Xu and Wisnom [**?**] have all presented experimental and numerical modelling results for angle-ply laminates with standard thickness plies ($t_\mathrm{p} = 0.125\,mm$) that show an increase in delamination onset stress with reduced blocking of plies. The commercialisation of tow spreading technology [**?**] that allows ply thickness to be reduced below 0.125 mm has seen further improvements in damage suppression. Amacher et al. [**?**] showed experimentally that, for thin ply (areal weight of $30\,\mathrm{g/m^2}$) quasi-isotropic (QI) laminates, delaminations could be completely suppressed under tensile loading. This led to a 42% higher laminate strength than if plies were blocked to give the equivalent of a $300\,\mathrm{g/m^2}$ ply. Similar gains have been presented by Sihn et al. [**?**] and Yokozeki et al. [**?**], who both conducted extensive testing of QI laminates and established that thin ply laminates can effectively suppress delaminations before failure for a range of tests, including open-hole tension and fatigue.

Other work within HiPerDuCT, influenced by the work of Aveston et al. [**?** **?**], has demonstrated that pseudo-ductility can be achieved by hybridising thin plies of CFRP with standard thickness glass fibre prepreg (GFRP) to create a unidirectional (UD) hybrid laminate [**?** **?** **?** **?** **?**]. Loaded in uniaxial tension, delamination is suppressed and fragmentation of the carbon ply occurs, leading to more gradual failure. It has been shown that the behaviour is dependent on the properties of each material, the absolute thickness of the central CFRP plies and the thickness ratio between the two materials. Adjustment of these parameters yields a non-linear stress-strain response of a UD laminate that would not be possible without this hybridisation.

The thin ply angle-ply laminates investigated by Fuller and Wisnom [**?** **?**] have shown significantly higher failure strains than those of UD hybrid laminates. Thus, they are a very good replacement for the GFRP plies used in hybrid laminates. On the other hand, the GFRP used to date in [**?** **?** **?** **?**], a standard 0.125 mm thickness material, has not permitted the desired fine adjustments of thickness ratio, thus limiting performance. It is possible to remove this limit by using the thinnest available plies throughout the stacking

sequence. The material chosen to investigate this is as used in [**?** **?**], a Skyflex CFRP (designated USN020A, referred to hence as 'Skyflex') containing TR30 fibres (fibre modulus, $E_\mathrm{f} = 235\,\mathrm{GPa}$ [**?**]) and K50 epoxy (Skyflex proprietary resin [**?**]), with a nominal ply thickness, $t_\mathrm{p} = 0.03\,\mathrm{mm}$. Use of the same material throughout, however, means that the laminate can not remain UD, as a difference between the strains to failure of the central and surrounding plies is required. To overcome this and to exploit their highly non-linear stress-strain behaviour, angle-ply layers are to replace the GFRP plies used in [**?** **?** **?** **?**]. The high pseudo-ductile strains and damage suppression demonstrated by the angle-ply laminates in [**?** **?**] make this configuration an excellent candidate for the high strain material required in these hybrid systems.
This paper introduces an analytical model that allows a straightforward method to be used to predict the stress-strain response and damage modes of a $[\pm\theta_\mathrm{m}/0_\mathrm{n}]_\mathrm{s}$ laminate. These predictions are then validated against experimental results and post-failure inspection is performed via X-ray computed tomography (XCT). Further XCT is performed on interrupted specimens, giving insight into the development of damage over the entire loading.

2. Analytical modelling

The analytical modelling procedure presented combines the method used to predict the pseudo-ductile stress-strain behaviour of $[\pm\theta_\mathrm{m}]_\mathrm{s}$ laminates in [**?**] with the approach taken by Jalalvand et al. [**?**] for UD glass-carbon hybrid laminates. The model has been coded in MATLAB® and is a non-linear, iterative approach that accounts for the fibre rotation of the angle-ply layers, matrix plasticity and the possible 'hybrid' laminate damage modes, as discussed in [**?** **?** **?**].
There are three damage modes that can occur in these $[\pm\theta_\mathrm{m}/0_\mathrm{n}]_\mathrm{s}$ laminates: fracture of the 0° plies (Figure **??**); delamination at the 0/-θ interface (Figure **??**), and failure of the $\pm\theta$ plies (Figure **??**). Each one shall be presented in turn, giving the reasons for their occurrence and respective equations, as used in the analytical modelling.

2.1. Failure of 0° plies

Fracture of the central 0° plies will always occur first, with the subsequent damage progression depending on the material properties, absolute thickness of the 0° plies, t_UD and the thickness ratio of 0°:$\pm\theta$ plies, $B = t_\mathrm{UD}/t_\mathrm{AP}$.
Failure of the 0° plies is governed by the failure strain in the fibre direction, ϵ^*_{11}. The stress-strain response of these plies is assumed to be linear-elastic in the fibre direction, so once the fibre direction ply stress, σ_{11}, is sufficient that the inequality $\sigma_{11}/E_{11} \geq \epsilon^*_{11}$ is satisfied, the first failure in the 0° plies is deemed to have occurred. If the strength of the $\pm\theta$ plies is sufficient to withstand the stress redistribution created by the 0° failure, then further strain can be taken by the laminate. If, however, the $\pm\theta$ is not sufficiently strong, then complete failure of the specimen will occur without the development of any non-linearity.

2.2. Fragmentation

To determine if multiple fracture (termed 'fragmentation') of the 0° plies can occur, a unit cell (Figure **??**) is used to calculate the stress in the $\pm\theta$ layers at the point of 0° fracture and then compare that with a known strength for that $\pm\theta$ layup. It is assumed that the

damage is symmetric about the mid-plane, thus the unit cell represents half the laminate thickness and all definitions of thickness are in accordance with this half thickness. The stress in the angle-plies away from the 0° fracture is denoted as σ_x^{AP}. The stress at the crack, σ_{crack}, is calculated using the effective reduced cross-section of the laminate after the fracture of the 0° plies. A stress concentration factor of $K_t = 1.08$, as used in [**?**], is included to account for the local stress increase at the crack tip:

$$\sigma_{\mathrm{crack}} = K_t \sigma_x \left(\frac{t}{t_{\mathrm{AP}}} \right), \tag{1}$$

where σ_x is the laminate applied stress, t_{AP} is the thickness of the angle-ply layers and t is the laminate thickness ($t = (t_{\mathrm{AP}} + t_{\mathrm{UD}})$, noting that these pertain to the half thickness). At initial 0° fracture, the values of applied stress, σ_x and strain, ϵ_x, (away from the crack) are referred to as σ_{frag} and ϵ_{frag} respectively. The value of σ_{crack} is compared to the known strength for that $\pm\theta$ layup, which is established beforehand and stored using the method set out in [**?**].

If failure of the laminate does not occur at this point, then the stress away from the crack in the unit cell is assessed. The value of this stress depends on the width of the unit cell, which can be taken to be equivalent to the spacing of the fragmentations. For each stacking sequence, there exists a critical spacing between cracks, known as the critical length, l_{c}. The value of l_{c} can be determined by considering, in a similar manner to Aveston et al [**?**], the force-balance relation between the fractured 0° ply and the shear stress transferred at the 0/-θ interface:

$$l_{\mathrm{c}} = \frac{2\sigma_{11}^{*} t_{\mathrm{UD}}}{\tau_{\mathrm{Y}}}. \tag{2}$$

It is assumed that the matrix is an elastic-plastic material giving a constant shear stress at the interface. The value of interfacial shear yield is assumed to be equivalent to the in-plane shear of $\tau_{\mathrm{Y}} = 55\,\mathrm{MPa}$, established via $[\pm 45_5]_{\mathrm{s}}$ tensile tests in [**?**]. It can be seen from Equation **??** that l_{c} is dependent on the thickness of the 0° plies and the strengths of the material in the fibre direction and in interfacial shear.

Figure **??** shows the variation of stresses for a laminate with multiple fractures in the 0° plies. The maximum value of stress in the angle-ply layers, σ_{crack}, is independent of the unit cell length. The value of σ_{AP} (shown in Figure **??**), however, is dependent on the crack spacing:

$$\Delta\sigma_{\mathrm{AP}} = \frac{l}{l_{\mathrm{c}}}(\sigma_{\mathrm{crack}} - \sigma_{\mathrm{AP}}). \tag{3}$$

It should be noted that the stress in the angle-ply layers close to the 0° fractures, σ_{AP}, is not equal to the effective far-field angle-ply stress, σ_x^{AP} and as such is an unknown. It can be found by relating σ_{crack} to the stress in the angle-ply immediately before fragmentation, σ_x^{AP}:

$$\sigma_{\mathrm{AP}} = \sigma_{\mathrm{crack}} + \frac{l}{l_{\mathrm{c}}} \left(\sigma_x^{\mathrm{AP}} - \sigma_{\mathrm{crack}} \right) where (0 < l < l_{\mathrm{c}}). \tag{4}$$

Equation **??** shows that σ_{AP} is effectively a mean of σ_x^{AP} and σ_{crack}. Due to the distribution of these stresses, fragmentations will only develop in regions of uniform stress. Assuming a constant fibre direction strength, this leads to the level of stress remaining constant over the course of fragmentations, creating a stress plateau from the point of initial fragmentation to saturation.

The stress between fragmentations in the 0° plies is dependent on their spacing in a similar way to the angle-ply stresses and can be expressed as:

$$\sigma_{\mathrm{UD}} = \frac{l}{l_{\mathrm{c}}}\sigma_{11}^{*}. \tag{5}$$

For the initial fragmentation, σ_{UD} is equal to the strength of the material in the fibre direction, σ_{11}^{*}, as shown in Figure **??**. Figure **??** presents how, as fragmentations develop, the proximity of the value of σ_{UD} to σ_{11}^{*} determines the value of fragmentation spacing, l. Fragmentation of the 0° plies continues until σ_{UD} is no longer uniform at any point along the length of the laminate and the material is broken into pieces of length between $l_{\mathrm{c}}/2$ and l_{c} [**?**]. At this point, the effective stiffness of the 0° plies is assumed to have reduced considerably. This is taken account of in the model by reducing the E_{11} of the 0° plies to maintain a constant level of applied stress. Due to the non-linearity of the response, establishing the strain at which this saturation of fractures occurs is performed via use of pre-calculated stress-strain responses found for the particular $\pm\theta$ layup. A linear stress distribution in the unit cell is assumed, so a linear interpolation between the values of σ_{crack} and σ_{AP} is performed. This gives a set of points that are matched to the $\pm\theta$ stress-strain curve, as shown in Figure **??**. These stresses yield equivalent strains, the distribution of which is plotted against the unit cell length, $0 \leq x \leq l$. Performing a numerical integration of this distribution gives the area under the curve, which is the elongation, δl, of the unit cell for that value of l, which in this work is assumed to be $0.75l_{\mathrm{c}}$. The value of l_c is layup dependent, as such l can not be known for each prediction, so $0.75l_c$ is selected as a mean of $0.5l_c$ and l_c, which are the theoretical minimum and maximum crack spacings respectively. The predicted strain of the laminate at fragmentation saturation is easily calculated via $\delta l/l$. This method removes the need to have knowledge of the stiffness of each layer, providing an accurate estimate of ϵ_x at saturation fragmentation.

2.3. Delamination

The initial fracture of the 0° plies creates a stress concentration that favours a Mode II delamination [**?**] at the 0/-θ interface. The stress at which this delamination occurs is governed by Equation **??**, which is adapted from [**?**],

$$\sigma_{\mathrm{del}} = \frac{1}{t_{\mathrm{AP}} + t_{\mathrm{UD}}}\sqrt{\frac{2G_{\mathrm{IIc}}E_x^{\mathrm{AP}}t_{\mathrm{AP}}(E_x^{\mathrm{AP}}t_{\mathrm{AP}} + E_{11}t_{\mathrm{UD}})}{E_{11}t_{\mathrm{UD}}}}, \tag{6}$$

where G_{IIc} is the critical strain energy release rate for Mode II delamination. An initial value of $G_{\mathrm{IIc}} = 1.0\,\mathrm{N/mm}$ has been set, using the value applied in [**?**] and [**?**]. The non-linear stress-strain response of the $\pm\theta$ layers leads to a non-constant value of E_x^{AP}, which is the modulus of these plies in the global x-direction. E_x^{AP} is taken as the secant modulus of the $\pm\theta$ ply stress and strain, σ_x^{AP} and ϵ_x^{AP}, as calculated by Classical Laminate Analysis (CLA). E_{11} is the modulus of the 0° plies in this configuration and does not vary throughout the loading. The respective thickness of each part of the laminate also influences the value of σ_{del}, where a decrease in t_{UD} for a fixed t_{AP} will lead to an increase in σ_{del}. The non-linearity and so reduction of E_x^{AP} leads to a decreasing value of σ_{del}, where its magnitude and rate of decrease depends on the original $\pm\theta$ fibre angle.
If the decrease in σ_{del} leads to it equalling the value of σ_{frag} at the point of initial fragmentation (ϵ_{frag}), then a large single delamination will occur at the 0/-θ interface. This

delamination is undesirable, as it causes a large load drop at the point of initial fragmentation. The laminate continues to take load, but at a lower level and its integrity is heavily diminished [**?**].
A better scenario comes about if $\sigma_{\text{frag}} < \sigma_{\text{del}}$, which means that fragmentations can develop first. The value of σ_{del} continues to reduce and once $\sigma_{\text{frag}} = \sigma_{\text{del}}$ at $\epsilon_x > \epsilon_{\text{frag}}$, dispersed delaminations will occur. In this case, delaminations are local to the fragmentations, propagating a short distance away from the fracture surface above and below the crack. As opposed to the single delamination, these local delaminations are stable and result in no drop of stress immediately after ϵ_{frag}.
For simplicity, these dispersed delaminations are assumed in the model to take place separately from fragmentations. In reality they are more closely linked and delaminations develop with the accumulation of fragmentations. It is further assumed that delaminations continue to develop until the entirety of the 0/-θ interface is debonded. At this point, the fragmented and delaminated 0° plies carry zero load, with the $\pm\theta$ plies taking the applied load. The strain limit of dispersed delamination is straightforward to predict for linear material responses, as presented in [**? ?**]. A similar method is not possible in this case, as the effective stiffness of both the 0° and $\pm\theta$ layers will change during delamination propagation. To establish the strain reached for the completion of delaminations, the value of E_{11} for the 0° plies is reduced at every strain increment until it reaches zero, at which point the model deems delaminations to have completed. In this way, similarly to reduction of E_{11} described for fragmentations, the stress at which delamination occurs is kept constant and the contribution of the 0° layers is gradually reduced. While this approach is not fully accurate, it is deemed to be sufficiently representative of the effective contribution of the 0° plies.

2.4. Failure of $\pm\theta$ plies

Failure of the $\pm\theta$ plies results in complete failure of the laminate and can occur, as mentioned in Section **??**, at the point of initial fragmentation or at any point following the saturation of fragmentations.
In general, this failure mode depends on the absolute and relative thickness of the 0° plies. If either of these are too large then the stress offloaded to the $\pm\theta$ layers at failure of the 0° will be in excess of the $\pm\theta$ strength, σ^*_{AP}. An estimate of the maximum value of the 0°:$\pm\theta$ thickness ratio, $B_{\max}$, can be made using Equation **??**, which is adapted from [**?**],

$$B_{\max} = \frac{\sigma^*_{\text{AP}}}{K_t \sigma^*_{11}} - \frac{E^{\text{AP}}_x}{E_{11}}. \tag{7}$$

This relationship shows that the maximum relative thickness of 0° plies for a given value of $\pm\theta$ is governed by the ratio of their strength and stiffness. The value of E^{AP}_x used is the initial tangent modulus value from the stress-strain response for a particular $\pm\theta$, which gives a conservative measure of $B_{\max}$. This is due to the higher relative thickness of angle-ply layers that results from a low $B_{\max}$, which means that the stress transferred to the $\pm\theta$ plies at fragmentation will be less than σ^*_{AP}.
The failure of the $\pm\theta$ plies is checked at initial fragmentation, as described in Section **??**. Subsequent checks for failure are performed following fragmentation saturation. It is assumed in the model that past this point in the loading, the angle-plies are carrying the majority of the load on the laminate. Indeed, following complete delamination of the 0/-θ interface, the $\pm\theta$ plies take all the applied load. Failure is deemed to have occurred in the

$\pm\theta$ layers and therefore in the complete laminate, if the following is true:

$$\sigma^*_{\mathrm{AP}} \leq \sigma_{\mathrm{AP}} = \sigma_x \frac{t}{t_{\mathrm{AP}}}. \tag{8}$$

If Equation **??** is satisfied, the model halts without additional increments and stores all relevant stress-strain data.

3. Initial analytical predictions

The determination of promising configurations is guided by using Equation **??** to find the value of $B_{\max}$ for a particular $\pm\theta$. The value of θ in this case was 26°. The previous work on thin ply angle-ply laminates presented in [**?**] has shown this fibre angle to be near optimal, in terms of E_x, σ^*_x and ϵ_{d}, for the Skyflex material in question. It should be noted that the current values of the elastic constants are lower than those established in [**?**]. It was found, following microscopy of specimens manufactured for the current work, that the fibre volume fraction, v_f, was lower than the previous batches of material, measuring approximately 35%. The values of strength and stiffness have been adjusted accordingly using the rule of mixtures. Equation **??** requires the strength and stiffness of both the 0° and $\pm\theta$ layers. The value of E_{11} is given in Table **??**, alongside the other elastic constants of E_{22}, G_{12} and ν_{12}. A failure strain of 1.9% is used for the TR30 carbon fibres, as established by Czél et al [**?**] for glass-carbon thin ply hybrid laminates. Assuming a linear-elastic response in the fibre direction, this leads to a σ^*_x of 1600 MPa. The values of $E^{AP}_x = 29\,\mathrm{GPa}$ and $\sigma^*_{AP} = 850\,\mathrm{MPa}$ have been calculated via the model introduced in [**?**]. Feeding these values into Equation **??** leads to a $B_{\max} = 0.186$. Given that $B = t_{\mathrm{UD}}/t_{\mathrm{AP}}$, for a single ply of 0° (where $t_{\mathrm{p}} = 0.03\,\mathrm{mm}$) it is found that at least 6 off-axis plies are required to avoid complete failure of the laminate at the point of initial fragmentation. This means that, for a symmetric laminate, 3 plies are needed either side of the 0°. If pairs of $\pm\theta$ plies are to be used, however, this is obviously not possible so the total number of angle-ply layers has been increased to 8, allowing two pairs of $\pm\theta$ each side of the 0° in a $[\pm 26_2/\underline{0}]_{\mathrm{s}}$ configuration ($B = 0.125$). To investigate the effects of doubling the number of 0° plies whilst maintaining the 1:8 ratio, a further layup of $[\pm 26_4/0]_{\mathrm{s}}$ is also modelled and presented with the $[\pm 26_2/\underline{0}]_{\mathrm{s}}$ layup in Figure **??**.

The analytical model introduced in [**?**] consistently yielded a small over-prediction of angle-ply laminate strength compared to the mean experimental results — approximately 20 MPa for $[\pm 26_5]_{\mathrm{s}}$. The current modelling procedure relies on these strength values in order to determine the point of failure, as discussed in Section **??**. With this in mind, the decision was taken to also predict the response of a more conservative configuration. The addition of a further pair of $\pm\theta$ plies reduced the ratio to 1:12 ($B = 0.08$) for the single 0° ply layup and 1:10 ($B = 0.1$) for the double 0° layup. As before, laminates containing both one and two 0° plies were modelled, giving layups of $[\pm 26_3/\underline{0}]_{\mathrm{s}}$ and $[\pm 26_5/0]_{\mathrm{s}}$. The stress-strain curves for these layups are also shown in Figure **??**. Due to the slightly different values of B, it can be seen that σ_{frag} is not the same for each laminate. This also highlights the trend of σ_{frag} to decrease with the reduction of B, where every pair of $\pm\theta$ added effectively reduces the performance of the laminate in terms of the stress at the onset of fragmentation.

There are noticeable differences in the amount of strain the laminates exhibit during each stress plateau. The plateaux of the $[\pm 26_2/\underline{0}]_{\mathrm{s}}$ and $[\pm 26_3/\underline{0}]_{\mathrm{s}}$ laminates, containing only one 0° ply, do not extend as far as the layups with an additional 0°. This is due primarily to

the damage development after the initial fragmentation. The layups with a single layer of 0° do not delaminate at the 0/-26 interface, exhibiting only fragmentation. The value of σ_{del} is higher than σ^*_{AP} throughout the loading, and so fragmentation saturation occurs, followed directly by a further increase in stress up to failure of the laminate. Slightly different stress-strain responses are shown by the $[\pm 26_4/0]_{\text{s}}$ (1:8) and $[\pm 26_5/0]_{\text{s}}$ (1:10) layups. These layups exhibit both fragmentations and local delaminations ($\sigma_{\text{del}} \leq \sigma_{\text{frag}}$ when $\epsilon_x > \epsilon_{\text{frag}}$), reaching a higher strain at both the end of the stress plateau and at failure compared to the layups that only fragment. It follows from these initial predictions that in order to maximise the pseudo-ductility of these configurations, it is necessary to promote local dispersed delaminations at the 0/-26 interface.

4. Experimental testing: proof of concept

Having performed the above predictions, it is important to validate the modelling by performing experimental testing. All four configurations give promising stress-strain results, but only two have been selected for testing. These were the thicker layups of each B ratio, the 1:8 $[\pm 26_4/0]_{\text{s}}$ ($t = 0.54$ mm) and 1:10 $[\pm 26_5/0]_{\text{s}}$ ($t = 0.66$ mm). In both cases, as above, the -26° plies are adjacent to the 0° plies. These were primarily selected due to the prediction of both fragmentation and delaminations that leads to additional pseudo-ductility. Secondary to this, the laminates containing only one 0° ply are considerably thinner, having nominal thicknesses of 0.27 mm and 0.39 mm. The low thickness of these laminates makes them fragile and so hard to handle and machine into test specimens without damaging them.

4.1. Test methodology

The material used for these laminates was the Skyflex spread tow CFRP introduced in Section **??**, maintaining consistency with previous thin ply angle-ply work in [**?** **?**]. Specimen size was also kept consistent with this previous work: gauge length of 150 mm and width of 15 mm, with GFRP cross-ply end tabs of 40 mm. Five specimens of each layup were manufactured via hand-layup, autoclave cured and then tested under uniaxial tensile loading. Longitudinal and transverse strains have been recorded using the Imetrum video extensometry system and associated software. All tests were performed using a Shimadzu AGS-10kNXD mechanically-actuated machine, under displacement control at 2 mm/min.

4.2. $[\pm 26_4/0]_{\text{s}}$ *results*

The stress - strain behaviour exhibited by the 1:8 specimens was more variable than anticipated. Figure **??** shows that only two of the tested specimens displayed the sort of stress plateau that was predicted by the modelling. The remainder of the batch all failed in a more catastrophic manner, where large drops in stress after the initial fragmentation rapidly led to further decreases of stress before complete failure of the specimen. This behaviour is similar to the results presented by Czél et al [**?**] for 0° hybrid specimens that exhibited a single delamination before failure — suggesting that the same damage could have occurred in this case also. Some specimens do, however, show a short stress plateau, which suggests that some fragmentations may have also occurred before failure of the ±26° plies.

It is recalled that Equation **??** determines the value of B using the relative strength and stiffness of the $\pm\theta$ and 0° plies assuming that the material is consistent and the specimens

are free of defects — such as fibre misalignment, voids or variation in fibre areal weight. These factors, as well as any misalignment of the specimen in the grips of the test machine, may contribute to locally altering this B ratio. This variation could cause damage mode to swap from the predicted fragmentation to a single delamination. These results effectively expose a limit of exploitation for the current layup, as there is not sufficient margin between the fragmentation stress and strength to allow a confident prediction.
Correlating the results with the modelling, Figure **??** shows that the fragmentation stress, σ_{frag}, and σ_x^* are well matched to the two specimens that showed pseudo-ductility, the strain at which further loading of the laminate occurs is very similar to experimental. It is interesting to note the tight margin between σ_{frag} and σ_x^*, for both the experimental and predicted results. For this layup the difference is not large — 55 MPa for the experimental and a predicted difference of 73 MPa. Table **??** suggests that the predicted ϵ_{d} and ϵ_x^* for the $[\pm 26_4/0]_{\text{s}}$ are not very accurate. This is due to the premature failure of three of the five specimens tested, evidenced by the large CV already discussed. If these three results are removed, leaving the specimens that behaved as predicted, the mean ϵ_{d} and ϵ_x^* are increased: $\epsilon_{\text{d}} = 2.20\%$ (CV = 7.3%) and $\epsilon_x^* = 3.88\%$ (CV = 5.3%), which are much closer to the predicted values shown in Table **??**. The modulus of the final section of the curve is predicted to be higher than the experimental. This behaviour, while not ideal, is consistent with the results presented in [**?**], as both models use the same formulation for the prediction of the non-linear angle-ply response.

4.3. $[\pm 26_5/0]_{\text{s}}$ *test results*

Figure **??** shows that the stress-strain behaviour of the 1:10 $[\pm 26_5/0]_{\text{s}}$ specimens was much more consistent. Four out of the five specimens tested display a stress plateau and portion of reloading of the laminate up to complete failure of the specimen. The one specimen that did not show a constant stress plateau (#2, red line on Figure **??**) follows an undulating path after the initial fragmentation of the 0° plies. The failure of the specimen also occurs much earlier, with the stress never exceeding the level of the first decrease. This behaviour could be down to misalignment in the test machine or a material defect. If treated as anomalous and removed from the sample, the mean σ_x^* and ϵ_x^* shown in Table **??** increase to 826 MPa (CV = 1.14%) and 4.31% (CV = 2.84%) respectively. Interestingly, it can be seen that the margin between σ_{frag} and σ_x^* for this layup is larger than the $[\pm 26_4/0]_{\text{s}}$ laminate — 134 MPa experimentally and 123 MPa for the modelling.
Similarly to the $[\pm 26_4/0]_{\text{s}}$ layup, the predicted level of σ_{frag} is well matched to the experimental results, though the damage development is predicted to finish at a slightly lower strain. The final portion of the loading, as above, is predicted to be stiffer than the experimental. The strength is within the experimental distribution, but occurs at a lower ϵ_x^*. Table **??** shows that this under prediction of failure strain causes the ϵ_{d} predicted to also be lower than that achieved experimentally.
The above results have shown that these novel $[\pm\theta_{\text{m}}/0_{\text{n}}]_{\text{s}}$ layups, consisting of a single type of thin ply CFRP, are capable of producing a highly non-linear, pseudo-ductile stress-strain response. The modelling approach has also proved to be able to give predictions of sufficient accuracy that the method can be used as a straightforward pseudo-ductile design tool.

5. Damage mode analysis: X-ray Computed Tomography imaging

Analysis of the damage in the $[\pm 26_4/0]_{\text{s}}$ (1:8) and $[\pm 26_5/0]_{\text{s}}$ (1:10) specimens has been performed using XCT, in order to better understand the evolution of fragmentation and

delamination. All specimens were submerged in a zinc iodide solution dye penetrant to highlight any damage. All images were captured using a Nikon Xtek XT 225, set at 80 kV, 140 μA, with 2000 projections (2 frame averaging) at 250 ms exposure.

5.1. Damage in $[\pm 26_4/0]_s$ *specimens*

The inconsistency of the stress-strain behaviour of the $[\pm 26_4/0]_s$ (1:8) specimens has meant that only failed specimens were available for XCT imaging. Discussed in Section **??**, the specimens that failed prematurely all exhibited a distinct load drop immediately after the point of initial fragmentation. It is postulated that this occurs due to a combination of a single, large delamination at the 0/-26 interface and premature failure of the angle-plies. XCT scans have been conducted of two specimens that failed prematurely (#3, #4 as shown in Figure **??**) in order to establish if these delaminations are present. The resolution of the scans is 81 μm.

Figure **??** shows a large piece of specimen #3. It is clear that away from the point of fracture there are no fragmentations or delaminations. The inset shows in more detail the area around the fracture. The vertical, green line, labelled 'A', denotes the width position of the far right image, which gives a side view of the specimen. This image shows that there is a single large delamination at the mid-plane of the laminate that stretches down the length of the image.

Another piece of specimen #3 was also XCT scanned and is shown in Figure **??**. Conversely to the previous images, this section of the failed specimen shows some fragmentation and delaminations, both local and free-edge. Clearly, damage does not develop evenly over the entire gauge length. Consultation of Figure **??** reveals that the post-fragmentation stress-strain response for this specimen is a gradual decrease in σ_x before complete failure of the specimen. It is thought that the 0° plies could have fragmented over this strain, causing what is seen in Figure **??**. The red (top) and blue (bottom) boxes highlight each half of this area of the specimen. Inset 'A' gives a side view of the top half, again showing that there is a large delamination that extends from the point of failure. The bottom half, bounded in blue, is an image of the mid-plane (indicated by the red line in the far right side view). This front view shows that the fragmentations reside in the middle of the local delaminations around them. Also clear in this image are the bright, triangular sections that indicate the locations of free-edge delaminations at the innermost 26/-26 interface. Damage of this sort was not exhibited by the $[\pm\theta_5]_s$ specimens tested in [**?**], suggesting that the local delaminations at the 0/-26 interface provide a surface for crack propagation parallel to the fibres in the -26° ply, which then leads to a delamination at the 26/-26 interface.

Much like the larger piece of #3, specimen #4 in Figure **??** shows no ingress of dye penetrant away from the area of failure. The inset 'A' highlights that a large area of dye penetrant on the right hand side of the enlarged section corresponds to another delamination. This stretches away from the fractured area, but does not extend down the specimen as far as those seen in Figure **??**.

These XCT images suggest that the $[\pm 26_4/0]_s$ specimens failed following the large delaminations that propagated from the initial fracture of the 0° plies, meaning that limited, or no, fragmentations could develop.

5.2. Damage in $[\pm 26_5/0]_s$ *specimens*

To investigate the development of damage over the course of the stress plateau observed in Figure **??**, five $[\pm 26_5/0]_s$ specimens have been loaded to different points along the stress-strain graph as shown in Figure **??**. Each was then removed from the test machine

and submerged in zinc iodide dye penetrant. The strain values are: 1.50%, 2.00%, 2.50%, 3.00%, 3.75%. These values capture the laminate in various states, from undamaged through to saturation of fragmentations and dispersed delaminations.
Figure **??** presents images from XCT scanning for each specimen with the dye penetrant reflections highlighted in pink, clearly showing the development of damage. The images show the entire gauge length of each specimen and as such the resolution of these scans is 81 μm — almost three times the ply thickness. The three clusters of dots on each specimen are the markings used to capture strains in testing, not features of the specimens. Each stage of the stress-strain curve shall be dealt with in turn, describing the damage that develops. To aid this process, further scans of specimens #2 ($\epsilon_x = 2.0\%$) and #3 ($\epsilon_x = 2.5\%$), performed at a higher resolution of 29.6 μm, will be presented also. This resolution is the same as the ply thickness, which has produced much finer images, enabling detail at that level to be analysed.

1. *Interrupted at $\epsilon_x = 1.50\%$.* It is clear to see that, prior to the stress plateau, there is an absence of any discernible damage. This is not surprising, as the failure strain of the 0° plies has not been reached and the previous work on $[\pm 26_5]_s$ laminates showed suppression of damage until final failure.
2. *Interrupted at $\epsilon_x = 2.00\%$.* At this point, the stress plateau has been reached and from previous studies [**?** **?** **?**] fragmentation is expected to have initiated in the 0° plies. The more detailed XCT images in the yellow (top) and blue-bounded (bottom) images of Figure **??** indicate that this is indeed the case. These images are all captured at the specimen mid-plane, with the dye penetrant visualised in white. Some fragmentation has occurred at this strain and is visualised by thin dark lines stretching across the specimen width. The inclined, prominent white regions in the central, main image show that some fragmentations are surrounded by local delaminations around the cracks at the 0/-26 interface. Free-edge delaminations are also present at this stage of the loading. The lower intensity of these triangular regions suggests that the damaged areas are at a different level in the laminate than the local delaminations. This is confirmed by the red-bounded images on the left of Figure **??**, which show three different views of the specimen: a large plan view, image A looks along the length of the specimen in the loading direction and image B shows the side view. The returns from the dye penetrant in images A and B appear as two separate, thin lines of brightness at the ±26° interfaces nearest the mid-plane.
3. *Interrupted at $\epsilon_x = 2.50\%$.* Delaminations at the free-edge have increased and, in some cases, each triangular shape seems to join up with the thinner strips of white indicating local delaminations. This suggests that there is a migration of delaminations from the 0/-26 interface to the -26/26 interface near the edge of the specimen. Some of these local delaminations, in the top third of the specimen, are also close to spanning its width. Figure **??** shows four side views of specimen #3, each one at a different width position covering the area indicated by the red lines in the insets. The damage can be seen to be confined to the innermost plies of the laminate. This indicates that, despite the increased strain, the predominant influence on the progression of damage are the 0° plies and, as shown for $[\pm\theta_5]_s$ laminates in [**?**], the ±26° layers away from the mid-plane are undamaged and able continue to carry load.
4. *Interrupted at $\epsilon_x = 3.00\%$.* Figure **??** shows that local delaminations have propagated extensively at this strain when compared to the image taken for the specimen halted at $\epsilon_x = 2.5\%$, just 0.5% earlier in the loading. They can be seen to extend the width

of the specimen, in many, but not all instances, joining the apex of a triangular-shaped edge delamination. These strips of damage due to local delaminations emanate from the fragmentations of the 0° plies and, therefore indicate that the laminate is heavily fragmented.

5. *Interrupted at ϵ_x = 3.75%.* The laminate is, at this point, extensively damaged and would have been close to complete failure. It can be said that the load is carried predominantly by ±26° plies, with only the slivers of bonded 0° plies contributing. This is seen in the $[\pm 26_5/0]_s$ stress-strain curves of Figures **??** and **??**, where the further loading beyond the stress plateau takes place at a much decreased stiffness. The saturation of fragmentation is clear from the relative periodicity of the highlighted areas. Similarly to the specimens halted at lower strains, some of the free-edge delaminations appear to join with, or indeed propagate from the direction of the fragmentations.

Clearly seen in all of the XCT images are the inclination of the fragmentations and subsequent local delaminations. Measurement of a selection of the damaged areas gives an inclination angle of 45° to 53° from the global x-direction. Throughout the loading, τ_{12} is zero in the 0° plies so the fragmentations should occur perpendicular to the loading direction. This zero shear stress suggests that the apparent inclination of the fragmentations is not connected to a transmittance of shear stress from the surrounding −26° plies. Instead, closer inspection of the fragmentations in specimen #2 (shown in Figure **??**) reveals that they are stepped — fibre fractures occur perpendicular to the load alternated with splits parallel to the fibres. The red ellipses in Figure **??** highlight clear cases of this for separate fragmentations. Thus, it is this discontinuous fracture behaviour that, at a lower magnification, appears as a smoother, inclined path.
Analysis of the tested specimens has given a clear insight into the development of damage within these laminates and has clearly shown that the concept of combining angle-ply fibre rotation with fragmentation and dispersed delamination damage modes can achieve pseudo-ductility with CFRP laminates. X-ray computed tomography has allowed not only the locations of fragmentations and delaminations to be identified, but also the sequence in which they propagate over the course of the loading.

6. Conclusions

The concept of combining fibre rotations and fibre fragmentation via application of angle-ply laminates with central 0° plies to achieve high performance, metal-like stress-strain responses has demonstrated a pseudo-ducility of up to 2.2%. An analytical modelling method has been developed to predict the non-linear stress-strain behaviour of thin ply $[\pm\theta_m/0_n]_s$ laminates. The damage modes of 0° fragmentation, local delamination at the 0/-26 interfaces and fracture of the angle-ply layers have all been incorporated into a non-linear, iterative model that combines the approaches taken in [**?**] and [**?**]. The likelihood of these damage modes occurring and the order in which they do so has been shown to depend on the absolute thickness of the 0° plies and the relative thickness of the 0° and $\pm\theta$ plies. The thin ply material allows these parameters to be finely tuned, thus controlling the failure of the laminate. The redistribution of stress that takes place during fragmentation has been shown to lead to a metal-like stress-strain curve, where, following fragmentation initiation, a stress plateau is maintained until a section of increased loading up to laminate failure.

Initial predictions were performed using the fibre angle of $\pm 26^\circ$, established in [**?**] as the most promising in terms of achieving pseudo-ductility in angle-ply laminates of the Skyflex material. A thickness ratio of $B = 0.125$ (1:8 for 0°:$\pm\theta$) was predicted to yield a promising pseudo-ductility, exhibiting fragmentation and then local delaminations prior to failure. For this ratio of 1:8 a layup of $[\pm 26_4/0]_\mathrm{s}$ was predicted to reach a $\epsilon_\mathrm{d} = 2.01\%$, $\sigma_\mathrm{frag} = 708\,\mathrm{MPa}$ and $\sigma_x^* = 781\,\mathrm{MPa}$. Another layup $[\pm 26_5/0]_\mathrm{s}$ ($B = 1{:}10$) was also predicted to exhibit promising results, but in a more conservative configuration ($\epsilon_\mathrm{d} = 1.91\%$, $\sigma_\mathrm{frag} = 676\,\mathrm{MPa}$, $\sigma_x^* = 799\,\mathrm{MPa}$).
Experimental results have shown that a $[\pm\theta_\mathrm{m}/0_\mathrm{n}]_\mathrm{s}$ laminate can achieve considerable pseudo-ductile strain, successfully validating the modelling approach. The layup of $[\pm 26_5/0]_\mathrm{s}$ showed consistent results. A mean pseudo-ductile strain of 2.2% and $\sigma_\mathrm{frag} = 692\,\mathrm{MPa}$ were attained, each surpassing the predicted values. There was, however, some variability in the responses. From a batch of five, only two $[\pm 26_4/0]_\mathrm{s}$ specimens displayed the predicted stress-strain curve. The remainder all failed prematurely, which XCT scanning showed to be due to a combination of a single large delamination at the $0^\circ/-26^\circ$ interface and premature angle-ply failure. The consistent stress-strain responses of the $[\pm 26_5/0]_\mathrm{s}$ specimens allowed further interrupted tests to be performed, which, via XCT scanning, have led to an improved understanding of the fragmentation and local delamination damage development. Higher resolution XCT scans have also provided the opportunity for the morphology of the 0° fragmentations to be seen, indicating that fibre fractures occur perpendicular to the applied stress, but these are interspersed by longitudinal splits. The presence of both of these gives rise to the apparent inclined path of the fragmentations and local delaminations.
The analytical modelling has been shown to provide adequate predictions of the stress-strain response for these laminates. Damage analysis has also led to a thorough understanding of the development of fragmentation and delamination, providing the basis to further investigate the predictive capabilities of the modelling and extend the experimental work to cover other orientations and stacking sequences.

Acknowledgements

This work was funded under the UK Engineering and Physical Sciences Research Council (EPSRC) Programme Grant EP/I02946X/1 on High Performance Ductile Composite Technology in collaboration with Imperial College, London.

References

[1] Allaer K, De Baere I, Lava P, Van Paepegem W, Degrieck J. On the in-plane mechanical properties of stainless steel fibre reinforced ductile composites. Compos Sci Technol 2014;100:3443.

[2] Masania K, Geissberger R, Stefaniak D, Dransfeld C. Steel Foil Reinforced Composites : Study of Strength , Plasticity and Ply Size Effects. 20th Int. Conf. Compos. Mater. ICCM-20, Copenhagen: 2015.

[3] Callens MG, De Cuyper P, Gorbatikh L, Verpoest I. Effect of fibre architecture on the tensile and impact behaviour of ductile stainless steel fibre polypropylene composites. Compos Struct 2015;119:52833.

[4] Kazemahvazi S, Schneider C, Deshpande VS. A constitutive model for self-reinforced ductile polymer composites. Compos Part A Appl Sci Manuf 2015;71:329.

[5] Swolfs Y, Meerten Y, Hine P, Ward I, Verpoest I, Gorbatikh L. Introducing ductility in hybrid carbon fibre/self-reinforced composites through control of the damage mechanisms. Compos Struct 2015;131:25965.

[6] Swolfs Y, Shi J, Meerten Y, Hine P, Ward I, Verpoest I, et al. The importance of bonding in intralayer carbon fibre/self-reinforced polypropylene hybrid composites. Compos Part A Appl Sci Manuf 2015;76:299308.

[7] Stefano DR, Lorenzo I, Curtis Paul T. Experimental Investigation of the Mechanical Properties of Dry Microbraids and Microbraid Reinforced Polymer Composites. Compos Struct 2015;125:50919.

[8] Gautam M, Potluri P, Ogin S, Jain P, Centre NC, Centre NC, et al. Necking behaviour of flattened tubular braided composites. 20th Int. Conf. Compos. Mater. ICCM-20, Copenhagen: 2015.

[9] Fuller JD, Wisnom MR. Pseudo-ductility and damage suppression in thin ply CFRP angle-ply laminates, Compos Part A Appl Sci Manuf 2014; 69: 64–71.

[10] Fuller JD, Wisnom MR. Exploration of the potential for pseudo-ductility in thin ply CFRP angle-ply laminates via an analytical method. Compos Sci Technol 2015;112:8-15.

[11] Czél G, Wisnom MR. Demonstration of pseudo-ductility in high performance glass/epoxy composites by hybridisation with thin-ply carbon prepreg. Compos Part A Appl Sci Manuf 2013;52:23-30.

[12] Czél G, Jalalvand M, Wisnom MR. Development of pseudo-ductile hybrid composites with discontinuous carbon- and continuous glass prepregs. 16th Eur. Conf. Compos. Mater., Seville: 2014.

[13] Jalalvand M, Czél G, Wisnom MR. Numerical modelling of the damage modes in UD thin carbon/glass hybrid laminates. Compos Sci Technol 2014;94:39-47.

[14] Jalalvand M, Czél G, Wisnom MR. Damage analysis of pseudo-ductile thin-ply UD hybrid composites A new analytical method. Compos Part A Appl Sci Manuf 2015;69:83-93.

[15] Jalalvand M, Czél G, Wisnom MR. Parametric study of failure mechanisms and optimal configurations of pseudo-ductile thin-ply UD hybrid composites. Compos Part A Appl Sci Manuf 2015;74:123-31.

[16] OBrien TK. Characterisation of delamination onset and growth in a composite laminate. NASA Techincal Memorandum, NASA Langley; January 1981

[17] OBrien TK. Analysis of local delaminations and their influence on composite laminate behaviour. NASA Technical Memorandum, NASA Langley; January 1984.

[18] OBrien TK, Hooper S. Local delamination in laminates with angle ply matrix cracks, Part 1: tension tests and stress analysis. In: Stinchcomb WW, Ashbaugh NE, editors. Compos. Mater. Fatigue Fract. (ASTM STP 1156). Fourth, Philadelphia: American Society for Testing and Materials; 1993, p. 491-506.

[19] Wang ASD, Crossman FW. Initiation and Growth of Transverse Cracks and Edge Delamination in Composite Laminates Part 1. An Energy Method. J Compos Mater 1980; 14: 71-87.

[20] Crossman FW, Warren WJ, Wang ASD, Law GE. Initiation and Growth of Transverse Cracks and Edge Delamination in Composite Laminates Part 2. Experimental Correlation. J Compos Mater 1980; 14: 88-108.

[21] Leguillon D, Marion G, Harry R, Lecuyer F. The onset of delamination at stress-free edges in angle-ply laminates–analysis of two criteria. Compos Sci Technol 2001; 61: 377-382.

[22] Xu X, Wisnom MR. An experimental and numerical investigation of the interaction between splits and edge delaminations in $[+20_{\mathrm{m}}/-20_{\mathrm{m}}]_{ns}$ carbon / epoxy laminates. In: Proceedings of ECCM-15, Venice; June 2012.

[23] Kawabe K, Tomoda S, Matsuo T. Technology for Spreading Tow and its Application to Composite Materials. Part 1. A New Pneumatic Method for Spreading Carbon Tow. J Text Mach Soc Japan 1997;50:68-75.

[24] Amacher R, Cugnoni J, Botsis J, Sorensen L, Smith W, Dransfeld C. Thin ply composites: Experimental characterization and modeling of size-effects. Compos Sci Technol 2014;101:121-32.

[25] Sihn S, Kim R, Kawabe K, Tsai S. Experimental studies of thin-ply laminated composites. Compos Sci Technol 2007; 67: 996-1008.

[26] Yokozeki T, Aoki Y, Ogasawara T. Experimental characterization of strength and damage resistance properties of thin-ply carbon fiber/toughened epoxy laminates. Compos Struct 2008; 82: 382-9.

[27] Aveston J, Cooper GA, Kelly A. Single and multiple fracture. Prop. Fibre Compos., Guildford: National Physical Laboratory; 1971, p. 15-25.

[28] Aveston J, Kelly A. Theory of multiple fracture of fibrous composites. J Mater Sci 1973;8:35262.

[29] Aveston J, Kelly A. Tensile First Cracking Strain and Strength of Hybrid Composites and Laminates. Philos Trans R Soc London Ser A, Math Phys Sci 1980;294 :51934.

[30] Mitsubishi Rayon Co. Ltd. Pyrofil carbon fibre datasheet 2013.

[31] SKChemicals. Standard Resin: K 50 - datasheet and recommended cure cycle 2008.

[32] Cui W, Wisnom M, Jones MI. An experimental and analytical study of delamination of unidirectional specimens with cut central plies. J Reinf Plast 1994;13.

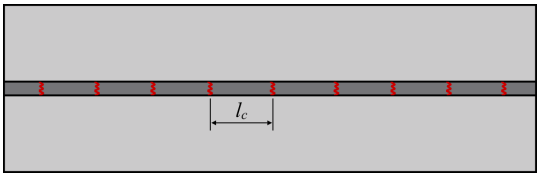

(a) Fragmentation of 0° plies.

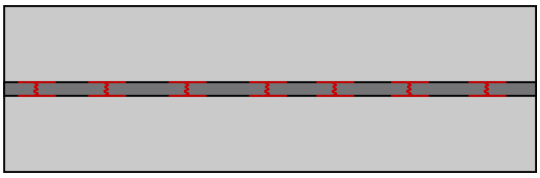

(b) Delamination of 0° — angle-ply interface.

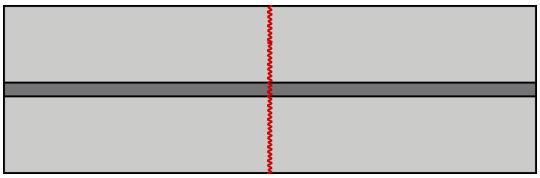

(c) Failure of the angle-plies after initial fragmentation of 0° layers.

Figure 1: Schematics show the three possible modes of damage that can occur in $[\pm\theta_m/0_n]_s$ laminates. l_c in **??** refers to the critical crack spacing.

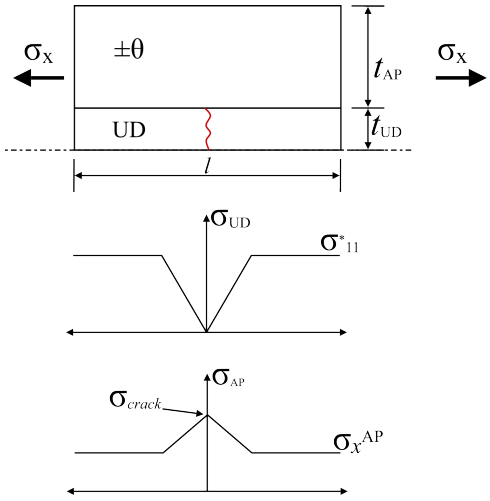

Figure 2: The unit cell, with a single fracture in the 0° plies, is shown. The graphs below indicate the idealised redistribution of stresses in the 0° and angle-ply layers.

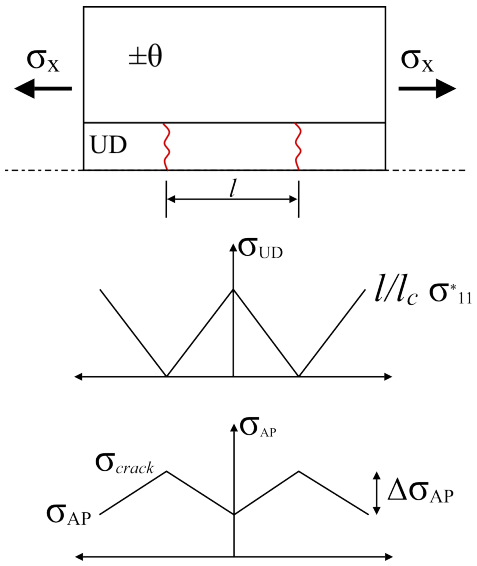

Figure 3: The redistribution of stress in the angle-plies and 0° layers is governed by the spacing of fragmentations in the 0°, l/l_c. Note that $\sigma_{\mathrm{AP}} \neq \sigma_x^{\mathrm{AP}}$ when $l \neq l_c$.

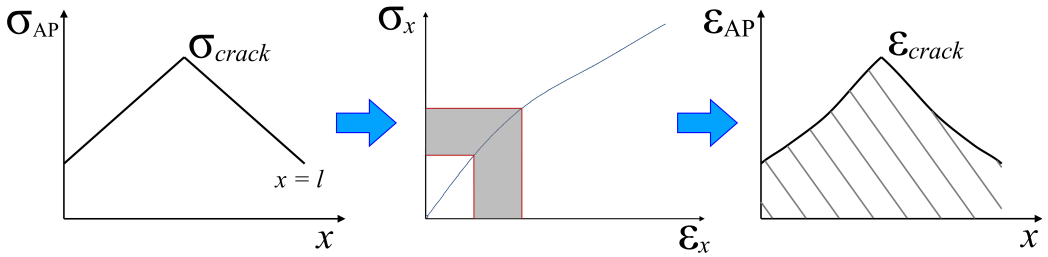

Figure 4: The σ_{crack} and σ_{AP} are matched to the stress-strain curve for the corresponding value of $\pm\theta$ to give the range of strain (shown by the grey shading on the central plot). This is then plotted against the unit cell length and a numerical integration to get the area under this curve (the grey hatching) yields the elongation of the unit cell, δl.

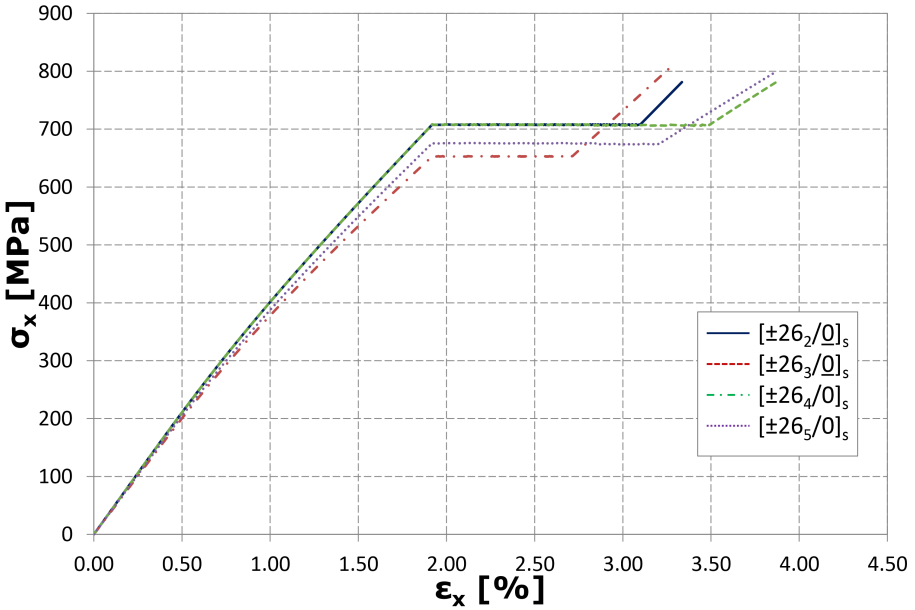

Figure 5: The predictions for $[\pm 26_m/0_n]_s$ laminates are shown. The effects of altering the thickness of 0° and ±26° layers can be seen from the different stress-strain behaviours following initial fragmentation.

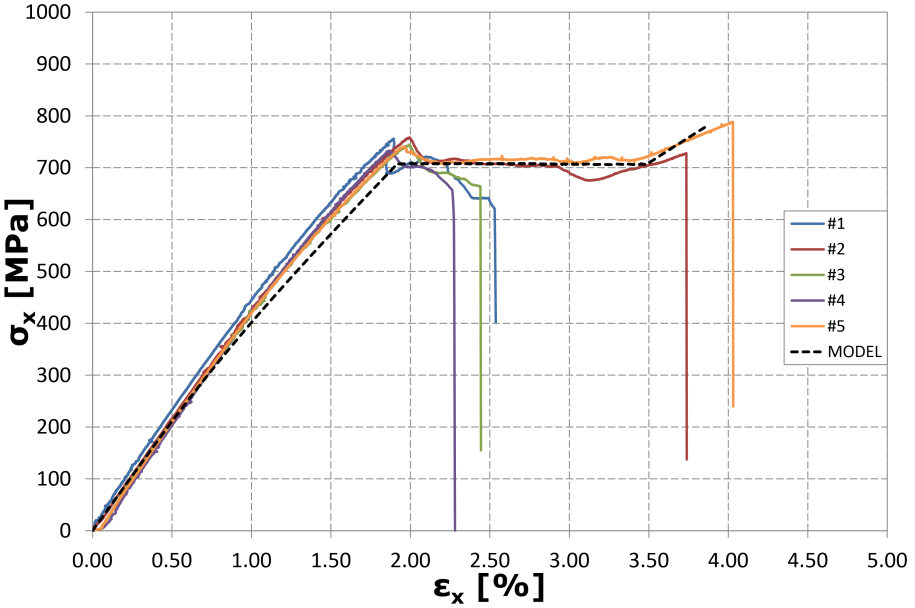

Figure 6: Experimental results for $[\pm 26_4/0]_s$, plotted with the initial analytical prediction (dashed line).

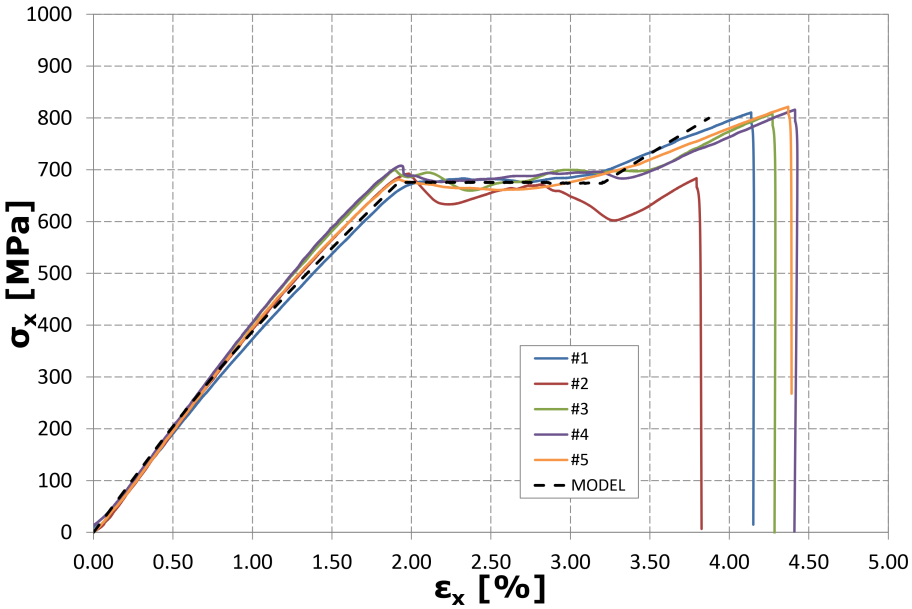

Figure 7: Experimental results for $[\pm 26_5/0]_s$, plotted with the initial analytical prediction (dashed line). The over-prediction of E_x is clear.

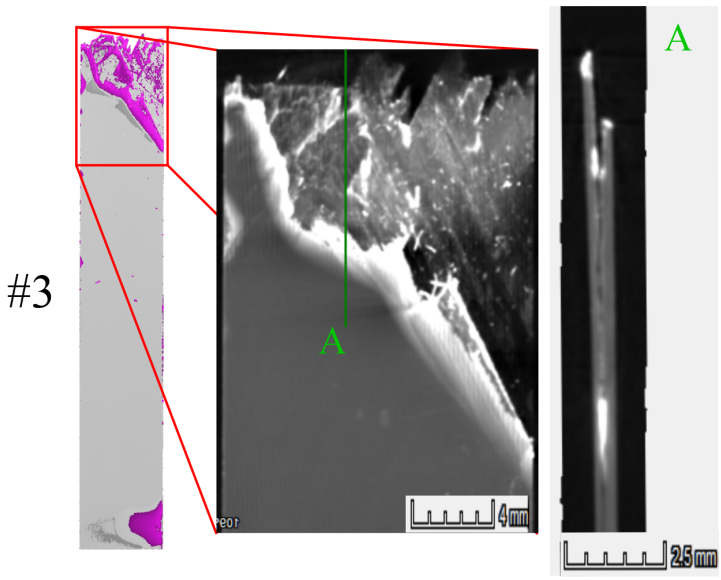

Figure 8: XCT images show that there is a complete absence of damage away from the part of the specimen where failure occurred. The inset 'A' shows also that a single delamination at the mid-plane extends away from the fracture.

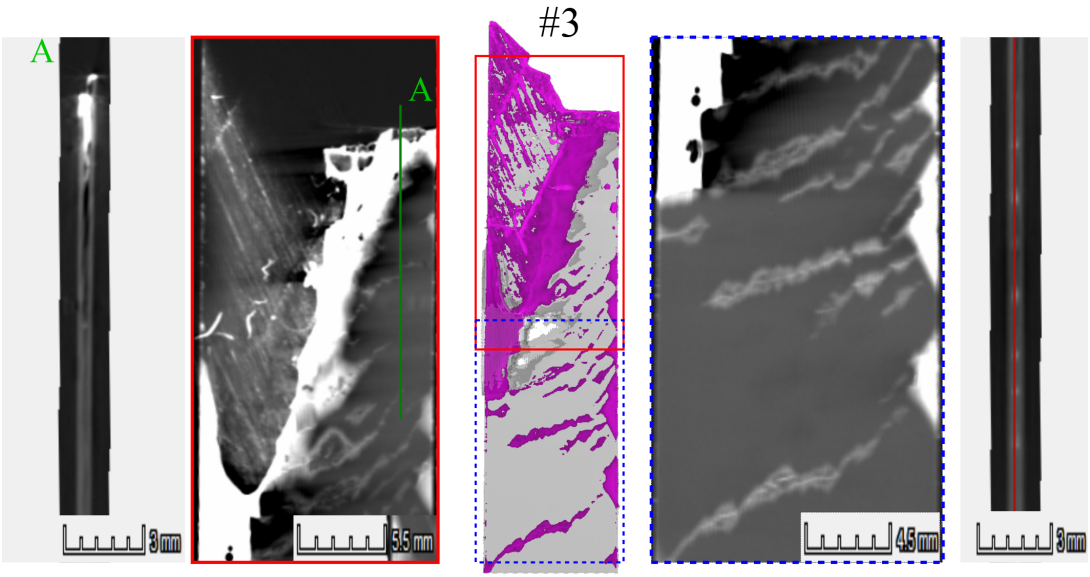

Figure 9: The XCT images detail the extent of the fragmentations and delaminations in a section of specimen #3 from $[\pm 26_4/0]_s$. The dashed box (right) shows clearly that fragmentations reside within the centre of the local delaminations. The inset image A shows a slice through the specimen, as indicated in the main image (solid bound). The rightmost image shows, via the solid vertical line, the thickness position of the dashed bound image.

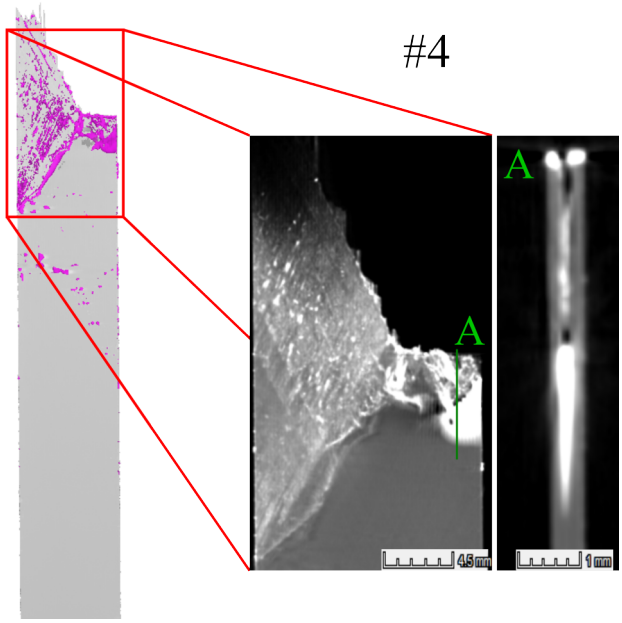

Figure 10: As shown in Figure **??**, the damaged area of the laminate is restricted to the immediate area around the fracture, indicating that no fragmentations developed prior to specimen failure.

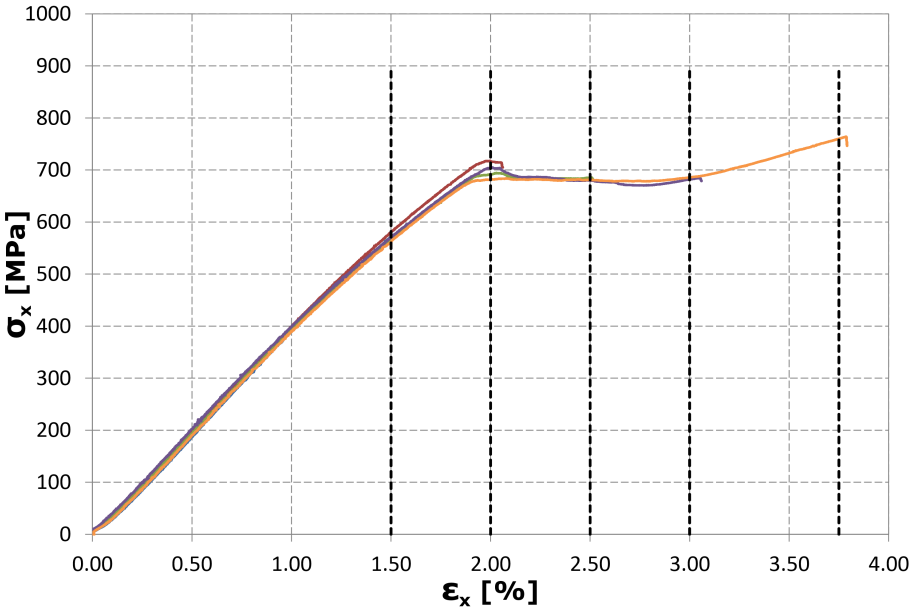

Figure 11: Stress-strain plot shows the five 1:10 laminates loaded to provide specimens for XCT scans. The vertical lines indicate where a specimen was halted and removed from the test machine.

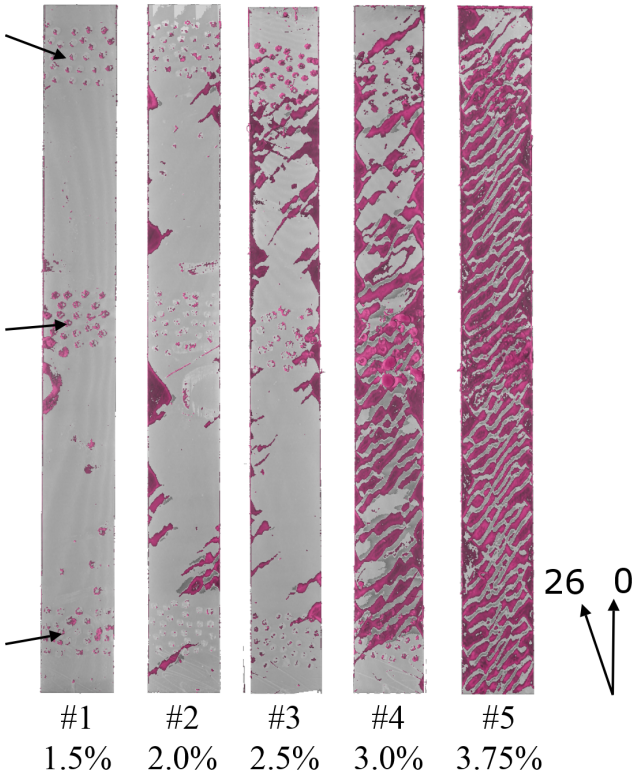

Figure 12: The five specimens are arranged in order of strain. The dye penetrant reflections are shown in pink. It should be noted that the arrows show the locations of dye has adhered to the markings used for strain measurements, which do not indicate damage.

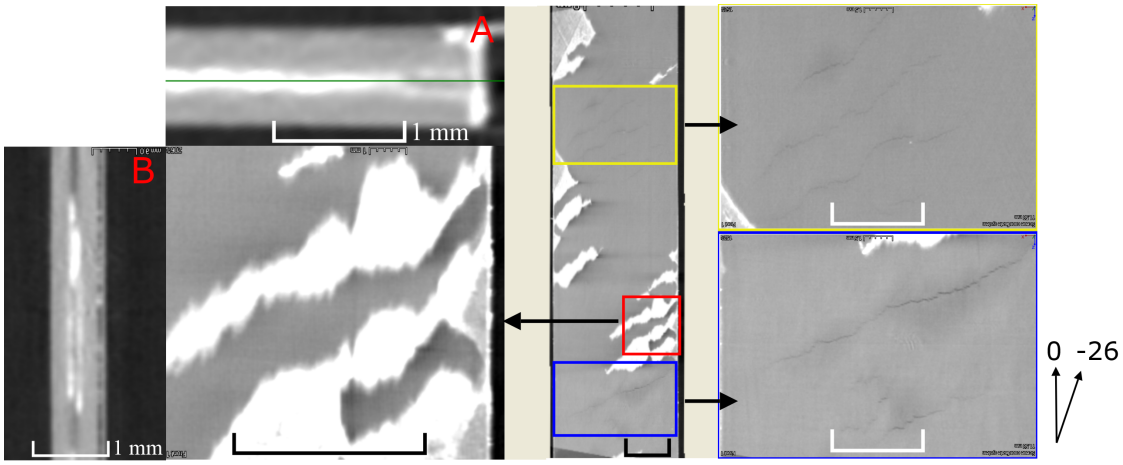

Figure 13: XCT images from the mid-plane of the laminate (#2, $\epsilon_x = 2.0\%$) highlight the development of fragmentations in the central 0° plies (blue and yellow surrounds). The red-bounded inset images show that dispersed and free-edge delaminations occur at different interfaces. The green line in A indicates the through-thickness position of the detailed red-bounded image. All scale bars are 5 mm, unless otherwise stated.

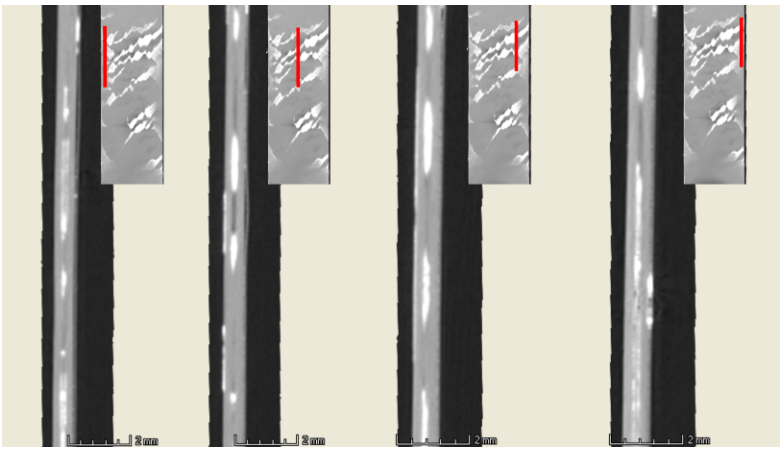

Figure 14: Images across the specimen width show that the damage is confined to the innermost plies of the laminate (#3, $\epsilon_x = 2.5\%$). The insets show the width position of each side view.

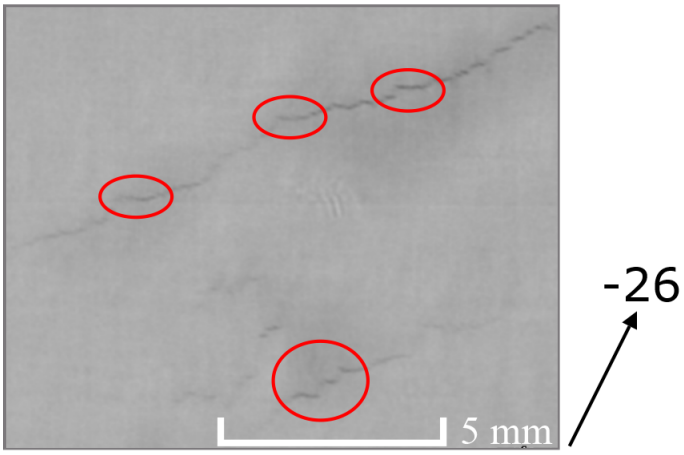

Figure 15: Closer inspection of the XCT images from the mid-plane of specimen #2 ($\epsilon_x = 2.0\%$) show that fragmentations in the central 0° plies occur as stepped process of fibre fracture and splitting, leading to an apparent inclination seen in other images. The red ellipses highlight positions of clear examples of this behaviour. The arrow indicates the adjacent ply angle.

Tables

Table 1: The elastic constants for Skyflex material at $v_f \approx 35\%$, as given by the model presented in [**?**].

E_{11}	84.4 GPa	E_{22}	5.48 GPa
G_{12}	2.27 GPa	ν_{12}	0.32

Table 2: Mean σ_x^*, σ_{frag}, ϵ_x^* and ϵ_{d} values for model and experimental results of 1:8 and 1:10 laminates. 'E' and 'M' are experimental and modelling respectively. 'E†' indicates that values are for the reduced batch size of two $[\pm 26_4/0]_{\text{s}}$ specimens, as discussed in Section **??**. The coefficient of variation (CV) appears in parentheses.

		$[\pm 26_4/0]_{\text{s}}$ (1:8)			$[\pm 26_5/0]_{\text{s}}$ (1:10)	
		E	E†	M	E	M
σ_x^*	[MPa]	756 (3.2%)	773 (2.8%)	781	801 (6.9%)	799
σ_{frag}	[MPa]	701 (5.2%)	685 (2.9%)	708	692 (1.6%)	676
ϵ_x^*	[%]	3.00 (27.2%)	3.88 (5.3%)	3.87	4.20 (5.8%)	3.87
ϵ_{d}	[%]	1.3 (66%)	2.20 (7.3%)	2.01	2.2 (7.4%)	1.91